

Spontaneous edge current in a small chiral superconductor with a rough surface

Shu-Ichiro Suzuki¹ and Yasuhiro Asano^{1,2,3}

¹Department of Applied Physics, Hokkaido University, Sapporo 060-8628, Japan

²Center for Topological Science & Technology, Hokkaido University, Sapporo 060-8628, Japan and

³Moscow Institute of Physics and Technology, 141700 Dolgoprudny, Russia

(Dated: December 3, 2024)

We study theoretically the spontaneous edge current in a small chiral superconductor with roughness at its surface. Under the self-consistent solutions of the pair potential and the vector potential obtained by solving the quasiclassical Eilenberger equation and the Maxwell equation simultaneously, we numerically calculate the spatial distribution of the chiral edge current in a small superconductor. The characteristic behavior of the spontaneous edge current depends strongly on the symmetry of the order parameter such as chiral p -wave, chiral d -wave and chiral f -wave pairing symmetries. The edge current is robust under the surface roughness in the chiral p - and chiral d -wave superconductors. In the chiral d -wave case, the surface roughness tends to flip the direction of the chiral current. On the other hand, the edge current in a chiral f -wave superconductor is fragile under the surface roughness. We also discuss the dependence of the spontaneous magnetization on temperature which is a measurable value in standard experiments.

PACS numbers: 73.20.At, 73.20.Hb

I. INTRODUCTION

Experimental detection of a spontaneous edge current could be a direct evidence of the chiral superconductivity. A number of Cooper pairs sharing a specific angular momentum carry the spontaneous edge current in chiral superconductors^{1,2} which can be measured as a spontaneous magnetization in experiments. Strontium ruthenate Sr_2RuO_4 is a leading candidate of a chiral p -wave superconductor^{3,4} whose pair potential is described by $\Delta(k_x + ik_y) = \Delta e^{i\chi\theta}$ in momentum space. Here $k_x = \cos\theta$ ($k_y = \sin\theta$) is the normalized wavenumber in the x (y) direction, and Δ is the amplitude of the pair potential. The topological Chern number $\chi = 1$ or -1 corresponds to the angular momentum of a Cooper pair. In addition to the chiral p -wave superconductivity, the possibilities of the chiral d -wave ($\chi = \pm 2$) and chiral f -wave ($\chi = \pm 3$) superconductivity have been discussed in recent experiments.⁵⁻¹⁴ Several theories have suggested that the amount of the edge current become smaller in chiral superconductor with larger $|\chi|$.^{15,16} So far, unfortunately, the spontaneous chiral current has never been observed in any experiments yet.^{17,18}

The absence of the spontaneous magnetization in experiments has been attributed mainly to two effects: (i) the Meissner screening of the edge current by the bulk superconducting condensate and (ii) the reduction of the chiral current by the potential disorder near the surface of a superconductor. The first effect was partially studied by Matsumoto and Sigrist.¹ They have confirmed a reduction of the edge current by the Meissner effect in a chiral p -wave superconductor theoretically. The resulting spontaneous magnetization, however, is large enough to be measured in experiments. The second effect is linked to an issue of the intrinsic angular momentum in ${}^3\text{He-A}$ phase.^{32,33} Experimentally it is difficult to make a superconducting sample with a specular surface. For

instance, a small cluster of a ruthenate superconductor is fabricated by using the focused ion beam technique,^{19,20} which would damage the sample quality near the surface seriously. So far several theoretical papers have suggested the presence of the edge states in a chiral p -wave superconductor under the surface roughness.^{21,22} At present, we have never known how the Meissner screening and the surface roughness reduce the edge current in chiral d - and f -wave superconductors. In previous papers,^{23,24} we have studied the Andreev bound states²⁵⁻³⁰ (ABSs) in time-reversal non-chiral superconductors characterized by $d_{x^2-y^2}$ -wave or p_x -wave pair potentials. We found that the ABSs in a p_x -wave superconductor is robust even in the presence of the surface roughness, whereas those in a d -wave one is fragile against the surface roughness. This conclusion is well explained by the symmetry of the Cooper pairs induced near the surface. However, it is unclear if it is possible to generalize our conclusions straightforwardly to chiral superconductors. We will address these issues in the present paper.

In this paper, we theoretically study the spontaneous edge currents and the spontaneous magnetization in a small chiral superconducting disk based on the quasiclassical Eilenberger formalism. By solving the Eilenberger equation and the Maxwell equation self-consistently and simultaneously, we obtain the spatial profiles of the chiral edge currents and the temperature dependences of the spontaneous magnetization. The surface roughness is considered through the impurity self-energy of a quasiparticle. We conclude that the robustness of the spontaneous edge current depends strongly on the paring symmetry. In a chiral p -wave superconductor, the amplitude of the chiral current in a disk with a rough surface is comparable to that in a disk with a specular surface. In a chiral d -wave superconductor, there are two edge channels in a disk with a specular surface. They carry the currents in the opposite directions to each other. In

the presence of the surface roughness, one channel near the surface disappears and the other channel far from the surface carries the robust chiral current. We show that the surface roughness changes the current direction in a chiral d -wave disk. The edge current in a chiral f -wave superconductor is fragile under the surface roughness. The effects of Meissner screening on the chiral edge current depend on the spatial current distribution near the surface. When the current decreases monotonically with the increase of the distance from the surface, the Meissner effect always reduces the chiral current. The Meissner effect is totally weak when the chiral current changes its direction as a function of the distance from the surface. Such complicated current distribution causes the self-screening effect among edge currents flowing in the opposite direction to one another.

This paper is organized as follows. In Sec. II, we explain the quasiclassical Eilenberger formalism and define the spontaneous magnetization of a small superconducting disk. In Sec. III, we present the results obtained by non-self-consistent simulations (i.e., with a homogeneous pair potential and without a vector potential). In Sec. IV, we discuss the spontaneous edge current in a superconducting disk with a *specular* surface. In Sec. V, we study the effects of surface roughness on the spontaneous edge current. In Sec. VI, we demonstrate the temperature dependence of the spontaneous magnetization which is a measurable value in experiments. In Sec. VII, we summarize this paper.

II. QUASICLASSICAL EILENBERGER THEORY

Let us consider a small chiral superconducting disk in two-dimension as shown in Fig. 1. We assume that there is no chiral domains by choosing the radius of the disk R to be comparable to the coherence length. We apply the quasiclassical Green function theory of superconductivity³¹ to calculate the edge current of a chiral superconductor. In an equilibrium superconductor, the Eilenberger equation takes the form

$$iv_F \mathbf{k} \cdot \nabla_{\mathbf{r}} \check{g} + [\check{H} + \check{\Sigma}, \check{g}]_- = 0, \quad (1)$$

where v_F is the Fermi velocity, \mathbf{k} is the unit wave vector on the Fermi surface, and $[\alpha, \beta]_- = \alpha\beta - \beta\alpha$. Throughout this paper, we use the set of units $\hbar = k_B = c = 1$, where $2\pi\hbar$ is the Planck constant, k_B is the Boltzmann constant, and c is the speed of light. The matrices \check{g} and \check{H} are defined as follows,

$$\check{g}(\mathbf{r}, \mathbf{k}, i\omega_n) = \begin{bmatrix} \hat{g}(\mathbf{r}, \mathbf{k}, i\omega_n) & \hat{f}(\mathbf{r}, \mathbf{k}, i\omega_n) \\ -\hat{f}(\mathbf{r}, \mathbf{k}, i\omega_n) & -\hat{g}(\mathbf{r}, \mathbf{k}, i\omega_n) \end{bmatrix}, \quad (2)$$

$$\check{H}(\mathbf{r}, \mathbf{k}, i\omega_n) = \begin{bmatrix} \hat{\xi}(\mathbf{r}, \mathbf{k}, i\omega_n) & \hat{\Delta}(\mathbf{r}, \mathbf{k}) \\ \hat{\Delta}(\mathbf{r}, \mathbf{k}) & \hat{\xi}(\mathbf{r}, \mathbf{k}, i\omega_n) \end{bmatrix}, \quad (3)$$

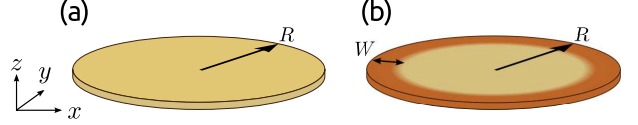


FIG. 1. Schematics of two-dimensional superconducting disks. The disk with a specular surface and that with a rough surface are shown in (a) and (b), respectively. The radius of the disk is denoted by R . The width of the disordered region is denoted by W in (b). We assume there is no chiral domain in the disk.

with $\hat{\xi}(\mathbf{r}, \mathbf{k}, i\omega_n) = [i\omega_n + ev_F \mathbf{k} \cdot \mathbf{A}(\mathbf{r})] \hat{\sigma}_0$, where $\omega_n = (2n + 1)\pi T$ is the Matsubara frequencies with n being an integer, T is the temperature, $\hat{\Delta}$ represents the pair potential, $\hat{\sigma}_0$ is the 2×2 identity matrix in spin space, and \mathbf{A} is the vector potential induced by the chiral edge current. We introduce the definition $\check{K}(\mathbf{r}, \mathbf{k}, i\omega_n) = K^*(\mathbf{r}, -\mathbf{k}, i\omega_n)$. The symbol $\check{\cdot}$ represents a 4×4 matrix structure in particle-hole space and the symbol $\hat{\cdot}$ represents a 2×2 matrix structure in spin space.

The effects of the rough surface are taken into account through the impurity self-energy, which is defined by

$$\check{\Sigma}(\mathbf{r}, i\omega_n) = \begin{cases} \frac{i}{2\tau_0} \int \frac{d\theta}{2\pi} \check{g}(\mathbf{r}, \theta, i\omega_n) & \text{for } r > R - W, \\ 0 & \text{for } r < R - W, \end{cases} \quad (4)$$

where $r = |\mathbf{r}|$ and θ is the angle between the unit vector \mathbf{k} and the x axis (i.e., $k_x = \cos \theta$ and $k_y = \sin \theta$), and τ_0 is the mean free time due to the impurity scatterings. The self-energy has finite values only near the surface as shown in Fig. 1(b), where W is the width of the disordered region. We consider three chiral superconductors with different pairing symmetries: spin-triplet chiral p -wave, spin-singlet chiral d -wave, and spin-triplet chiral f -wave pairing symmetries. In the spin-triplet superconductor, we assume that the pairing interactions work between two electrons with opposite spins. This assumption does not loose any generality of the argument below. The pair potential are described by

$$\hat{\Delta}(\mathbf{r}, \theta) = \begin{cases} \Delta(\mathbf{r}, \theta) \hat{\sigma}_1 & \text{for a spin triplet,} \\ \Delta(\mathbf{r}, \theta) i \hat{\sigma}_2 & \text{for a spin singlet,} \end{cases} \quad (5)$$

where $\hat{\sigma}_j$ for $j = 1-3$ are the Pauli matrices in spin space. The matrix Green functions in Eq. (2) can be represented by the scalar Green functions as

$$\hat{g}(\mathbf{r}, \theta, i\omega_n) = g(\mathbf{r}, \theta, i\omega_n) \hat{\sigma}_0, \quad (6)$$

$$\hat{f}(\mathbf{r}, \theta, i\omega_n) = \begin{cases} f(\mathbf{r}, \theta, i\omega_n) (-i \hat{\sigma}_1) & \text{for a triplet} \\ f(\mathbf{r}, \theta, i\omega_n) \hat{\sigma}_2 & \text{for a singlet.} \end{cases} \quad (7)$$

The pair potential in a chiral superconductor is described by

$$\Delta(\mathbf{r}, \theta) = \Delta_1(\mathbf{r}) \cos(\chi\theta) + i\Delta_2(\mathbf{r}) \sin(\chi\theta), \quad (8)$$

where Δ_1 and Δ_2 are the local amplitude of the two independent components. The topological numbers $\chi = \pm 1$, ± 2 , and ± 3 characterize the chiral p -, d -, and f -wave superconductivity, respectively. The doubly degenerate chiral superconducting states are indicated by $\pm\chi$. In this study, we consider superconducting states with positive χ . Deep inside a superconductor (i.e., bulk region), the relation $\Delta_1 = \Delta_2$ is satisfied. Therefore the pair potentials in the bulk are represented as

$$\Delta(\theta) = \bar{\Delta}(T)e^{i\chi\theta}, \quad (9)$$

where $\bar{\Delta}(T)$ is the amplitude of the uniform pair potential at a temperature T . In the simulations, Δ_1 and Δ_2 are self-consistently determined by the gap equation,

$$\begin{bmatrix} \Delta_1(\mathbf{r}) \\ \Delta_2(\mathbf{r}) \end{bmatrix} = N_0 g_0 \pi T \sum_{\omega_n} \int \frac{d\theta'}{2\pi} f(\mathbf{r}, \theta', i\omega_n) \begin{bmatrix} V_1(\theta') \\ V_2(\theta') \end{bmatrix} \quad (10)$$

where N_0 is the density of states per spin at the Fermi level. The coupling constant g_0 is determined by

$$(N_0 g_0)^{-1} = \sum_{n=0}^{n_c} \frac{1}{n + 1/2}, \quad (11)$$

where $n_c = (\omega_c/2\pi T)$ with ω_c being the cutoff energy. The functions V_1 and V_2 represent the attractive interactions as

$$V_1(\theta) = 2 \cos(\chi\theta), \quad V_2(\theta) = 2 \sin(\chi\theta). \quad (12)$$

The electric current $\mathbf{j}(\mathbf{r})$ is calculated from the Green function

$$\mathbf{j}(\mathbf{r}) = \frac{\pi e v_F N_0}{2i} T \sum_{\omega_n} \int \frac{d\theta}{2\pi} \text{Tr}[\check{T}_3 \mathbf{k} \check{g}(\mathbf{r}, \theta, i\omega_n)], \quad (13)$$

where $\check{T}_3 = \text{diag}[\hat{\sigma}_0, -\hat{\sigma}_0]$. The vector potential should be determined by solving the Maxwell equation,

$$\nabla \times \mathbf{A}(\mathbf{r}) = \mathbf{H}(\mathbf{r}), \quad (14)$$

$$\nabla \times \mathbf{H}(\mathbf{r}) = 4\pi \mathbf{j}(\mathbf{r}). \quad (15)$$

We iterate the Eilenberger equation for the Green function and the Maxwell equation for the vector potential to obtain the self-consistent solutions of $\Delta_1(\mathbf{r})$, $\Delta_2(\mathbf{r})$, $\mathbf{A}(\mathbf{r})$, and $\check{\Sigma}(\mathbf{r}, i\omega_n)$. In a finite size superconductor, we define the amplitude of the spontaneous magnetization M in terms of the spontaneous magnetic field $\mathbf{H}(\mathbf{r})$ as

$$M = \frac{1}{\pi R^2} \int_{r < R} d\mathbf{r} H(\mathbf{r}). \quad (16)$$

We start all of the simulations with the initial condition $\Delta_1(\mathbf{r}) = \Delta_2(\mathbf{r}) = |\bar{\Delta}(T)|$ and $\mathbf{A}(\mathbf{r}) = 0$, where $|\bar{\Delta}(T)|$ is the amplitude of the pair potential in a homogeneous superconductor at a temperature T . Throughout this paper, we fix several parameters: the radius

of a disk $R = 10\xi_0$, the cutoff energy $\omega_c = 6\pi T_c$ with T_c and $\xi_0 = \hbar v_F/2\pi T_c$ being the critical temperature and the coherence length, respectively. The magnetic field and the spontaneous magnetization are measured in units of the second critical magnetic field $H_{c2} = \hbar c/|e|\xi_0^2$. The current density is normalized to $j_0 = \hbar c^2/4\pi|e|\xi_0^3$. In the quasiclassical theory, the London length $\lambda_L = (mc^2/4\pi ne^2)^{1/2}$ is a parameter characterizing the spatial variation of magnetic fields, and is fixed at $\lambda_L = 5\xi_0$. In this paragraph, we explicitly denoted \hbar and c to avoid misunderstandings.

To solve the Eilenberger equation in a disk geometry, we apply the Riccati parametrization to the Green function^{34–36} and the technique discussed in Ref. 37. By using the Riccati parametrization, we can separate the Eilenberger equation into the two Riccati-type differential equations. Solving the Riccati equations along a long enough quasiclassical trajectory (typically 30 times of the coherence length), we can obtain the solutions of the Eilenberger equation.

As we will demonstrate in the following sections, the edge currents show complicated spatial profiles depending on the pairing symmetry. To analyze such behaviors, we decompose the electric current into a series of current components in terms of the symmetry of Cooper pairs. By using the normalization relation $g^2 - s_\nu \mathbf{f} \mathbf{f} = 1$ with the assumption $\mathbf{f} \mathbf{f} \ll 1$, we represent the normal Green function as $g \approx 1 + s_\nu \mathbf{f} \mathbf{f}/2$, where we have used the Eq. (7) and $s_\nu = 1$ ($s_\nu = -1$) for the spin-triplet (spin-singlet) pair potential. By substituting the expression into the current formula in Eq. (13), the electric current can be expressed as

$$\mathbf{j}(\mathbf{r}) = \sum_{\omega_n > 0} \mathbf{j}_{\omega_n}(\mathbf{r}) \quad (17)$$

$$\mathbf{j}_{\omega_n} = 4\pi e v_F N_0 T \int \frac{d\theta}{2\pi} \frac{1}{2} s_\nu \mathbf{k} \text{Im}[\mathbf{f} \mathbf{f}], \quad (18)$$

where we have used the relation $g(\mathbf{r}, \theta, i\omega_n) = -g^*(\mathbf{r}, \theta, -i\omega_n)$. Generally speaking, the pairing function $f(\mathbf{r}, \theta, i\omega_n)$ can be decomposed into the Fourier series

$$\begin{aligned} f(\mathbf{r}, \theta, i\omega_n) = & \sum_{a=0} f_a^c(\mathbf{r}, i\omega_n) \cos(a\theta) \\ & + \sum_{b=1} i f_b^s(\mathbf{r}, i\omega_n) \sin(b\theta). \end{aligned} \quad (19)$$

The surface breaks the inversion symmetry locally and induces the subdominant pairing components whose symmetries are different from that of the order parameter. In the absence of the vector potential, f_a^c and f_b^s are real functions. When we consider the current profile at $y = 0$,

Chiral p -wave	Chiral d -wave	Chiral f -wave
1	-	-
<u>$\cos \theta$</u> $\cancel{\text{---}}$ $\sin \theta$	$\cos \theta$ $\cancel{\text{---}}$ $\sin \theta$	$\cos \theta$ $\cancel{\text{---}}$ $\sin \theta$
$\cos 2\theta$ $\cancel{\text{---}}$ $\sin 2\theta$	<u>$\cos 2\theta$</u> $\cancel{\text{---}}$ $\sin 2\theta$	$\cos 2\theta$ $\cancel{\text{---}}$ $\sin 2\theta$
$\cos 3\theta$ $\cancel{\text{---}}$ $\sin 3\theta$	$\cos 3\theta$ $\cancel{\text{---}}$ $\sin 3\theta$	<u>$\cos 3\theta$</u> $\cancel{\text{---}}$ $\sin 3\theta$
$\cos 4\theta$ $\cancel{\text{---}}$ $\sin 4\theta$	$\cos 4\theta$ $\cancel{\text{---}}$ $\sin 4\theta$	$\cos 4\theta$ $\cancel{\text{---}}$ $\sin 4\theta$

— : Positive, - - - : Negative

FIG. 2. A chart of I_{ab} in Eq. (22). The diagonal lines connecting $\cos(a\theta)$ and $\sin(b\theta)$ indicate possible combinations of f_a^c and f_b^s for the chiral currents. The solid (broken) lines mean I_{ab} is positive (negative). The double underlines indicate the principal pairing component linking to the pair potential (i.e., $\cos(\chi\theta)$ and $\sin(\chi\theta)$). At the first line, “1” represents s -wave component.

the electric current in the y direction becomes

$$j_y(x) = \sum_{\omega_n} \sum_{ab} j_{ab}(i\omega_n) \quad (20)$$

$$j_{ab}(i\omega_n) = 4\pi|e|v_F N_0 T f_a^c f_b^s I_{ab} \quad (21)$$

$$I_{ab} = s_\nu(-1)^b(\delta_{b,1-a} + \delta_{b,a+1} - \delta_{b,a-1})/4 \quad (22)$$

where we use the relation $\tilde{f}(\mathbf{r}, \theta, i\omega_n) = f^*(\mathbf{r}, \theta + \pi, i\omega_n)$, and $\int d\theta \sin \theta \cos(a\theta) \sin(b\theta) = (\delta_{b,1-a} + \delta_{b,a+1} - \delta_{b,a-1})\pi/2$ for $a \geq 0$ and $b \geq 1$. The Kronecker’s δ functions appearing in Eq. (22) suggest that only the limited combinations of f_a^c and f_b^s contribute to the supercurrents, (e.g., $a = b \pm 1$). Moreover, the direction of the decomposed current j_{ab} in Eq. (21) depends on the relative signs among $f_a^c f_b^s$ and I_{ab} . Since the signs of $f_a^c f_b^s$ at a certain surface are turned out to be the same in most cases, the signs of I_{ab} mainly determine the current directions. We show a chart of $\text{sgn}[I_{ab}]$ in Fig. 2. The diagonal lines connecting $\cos(a\theta)$ and $\sin(b\theta)$ mean the possible combinations for carrying the currents. The solid (broken) lines indicate that I_{ab} is positive (negative). In a chiral p -wave superconductor, for example, I_{01} and I_{21} have the opposite signs to each other. As a result, the decomposed currents j_{01} and j_{21} flow in the opposite directions to each other.

III. NON-SELF-CONSISTENT SIMULATION

Before turning into effects of the surface roughness and those of the Meissner screening, the chiral currents under the uniform pair potential at $\mathbf{A} = 0$ should be summarized. The results presented in this section are qualitatively the same as those obtained by the Bogoliubov-de Gennes (BdG) formalism in Refs. 15 and 16.

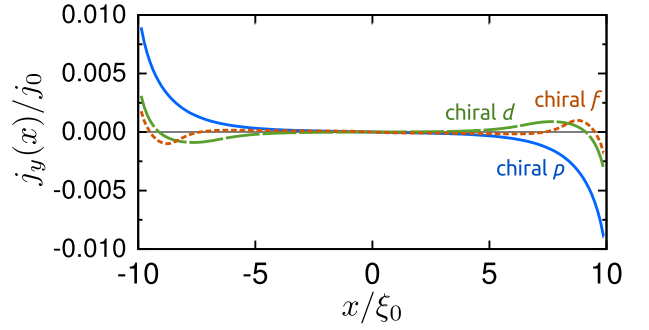


FIG. 3. Current densities in a disk of a chiral superconductor with a constant pair potential $\Delta_{1(2)}(\mathbf{r}) = |\bar{\Delta}(T)|$ at $\mathbf{A}(\mathbf{r}) = 0$, where $|\bar{\Delta}(T)|$ is the amplitude of the pair potential at a temperature T in a homogeneous superconductor. Here, we show the current distribution at $y = 0$. The radius of a superconducting disk, the temperature, and the cutoff energy are set to $R = 10\xi_0$, $T = 0.2T_c$, and $\omega_c = 6\pi T_c$.

The spatial dependences of the edge current are shown in Fig. 3, where we show the spatial distribution of the current in the y direction $j_y(x)$ at $y = 0$, where the temperature is set to $T = 0.2T_c$. The results are circular symmetric on a superconducting disk. In a chiral p -wave superconductor ($\chi = 1$), the amplitude of the edge current takes its maximum at $r = R$ and monotonically decreases with increasing the distance from the surface. When we observe the current from the $+z$ axis, the chiral current flows in the clockwise direction. The current distributions in chiral d -wave ($\chi = 2$) and chiral f -wave ($\chi = 3$) superconductors are rather complicated than that in a chiral p -wave case. The current density is negative (clockwise) around $x/\xi_0 = 10$ and is positive (counterclockwise) for $x/\xi_0 < 9$ in a chiral d -wave superconductor. In a chiral f -wave case, the cur-

rent density is negative for $9.5 < x/\xi_0 < 10$, positive for $7.8 < x/\xi_0 < 9.5$, and negative again for $x/\xi_0 < 7.8$. Such characteristic current distributions are related to the number of the edge channels (χ) and their decay length in the radial direction. Details are briefly summarized in Appendix A, where we analytically represent the wave function of the edge states for a semi-infinite chiral superconductor and supply the analytical expression of the current distribution. The net current density $J = \int_0^R dx j_y(x)|_{y=0}$ decreases with the increase of the chiral index χ because there are the two (three) current channels in a chiral d -wave (f -wave) superconductor and they carry the currents in opposite directions.

IV. DISK WITH A SPECULAR SURFACE

In this section, we discuss the current distribution of a chiral-superconducting disk with a specular surface under the self-consistent pair potentials and the vector potential. The results are obtained by solving the Eilenberger equation and the Maxwell equation simultaneously and self-consistently. In Sec. IV A, we consider only the self-consistent pair potential at $\mathbf{A} = 0$ in Eq. (3) to analyze the complicated spatial distribution of the chiral current. The results tell us the symmetry of a Cooper pair that carries the chiral current. The effects of self-induced magnetic fields are briefly discussed in Sec. IV B. The parameters are set to the same values used in Fig. 3.

A. Results under self-consistent pair potential at $\mathbf{A} = 0$

In Fig. 4, we show the spatial dependence of the pair potentials Δ_1 and Δ_2 . In a chiral p -wave superconductor, the pair potential Δ_1 is strongly suppressed, whereas Δ_2 is slightly enhanced near the surface as shown in Fig. 4(a). These suppression and enhancement are closely related to the formation of the surface ABSs. Namely, Δ_1 changes its the sign while the quasiparticle is reflected by a specular surface. These spatial variations of the pair potentials affect the edge current. The current density $j_y(x)$ at $y = 0$ in Eq. (20) is shown in Fig. 5(a). In a chiral p -wave disk, the edge current monotonically decreases with increasing the distance from the edge. The edge current in the self-consistent pair potential in Fig. 5(a) flows much wider area than that obtained by the uniform pair potential in Fig. 3. The range of “edge” is determined by the spatial variation of the pair potential in Fig. 4.

The surface breaks the inversion symmetry locally and the spatial variation of the pair potential breaks the translational symmetry. As a result, the subdominant pairing correlations are induced near the surface. In Fig. 2, we show the orbital symmetry of such subdominant components. The double underlines indicate the principal pairing component linked to the pair potential. At the first row, “1” represents s -wave symmetry. In a

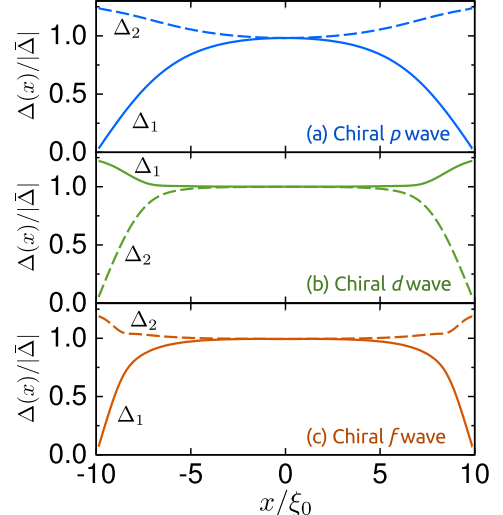


FIG. 4. Pair potentials in a disk of a chiral superconductor. The results are obtained by solving *self-consistently* the Eilenberger equation under the condition $\mathbf{A}(\mathbf{r}) = 0$. The superconducting disk is in the clean limit. The pair potentials are normalized to $|\bar{\Delta}(T)|$. The parameters are set to the same values used in Fig. 3.

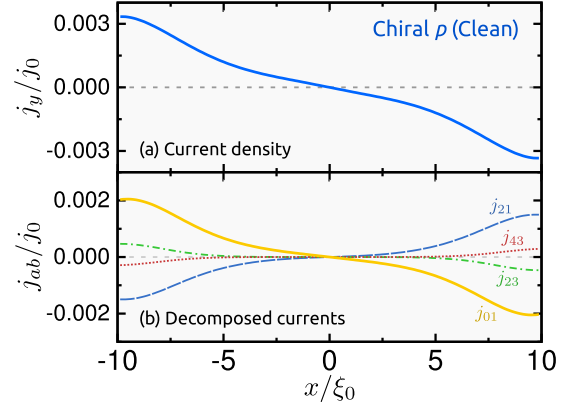


FIG. 5. Results for a chiral p -wave disk with a specular surface obtained by the self-consistent simulation under $\mathbf{A}(\mathbf{r}) = 0$. The current $j_y(x)$ in Eq. (20) at $y = 0$ is shown in (a). The component of $j_{ab}(\omega_0)$ at the lowest Matsubara frequency in Eq. (21) are shown in (b). The results are normalized to $j_0 = \hbar c^2 / 4\pi |e| \xi_0^3$. The parameters are set to the same values used in Fig. 3.

chiral p -wave case, the spatial variation of the principal component $\cos(\theta)$ induces the subdominant component such as s -wave, d -wave $\cos(2\theta)$, f -wave $\cos(3\theta)$, \dots . In the same way, the principal component $\sin(\theta)$ induces the subdominant component of d -wave $\sin(2\theta)$, f -wave $\sin(3\theta)$, \dots . The current is decomposed into the series of j_{ab} in Eq. (21). The results for a chiral p -wave disk are shown in Fig. 5(b), where j_{01} , j_{21} , j_{23} and j_{43} contribute mainly to the current. Here j_{ab} is calculated at the low-

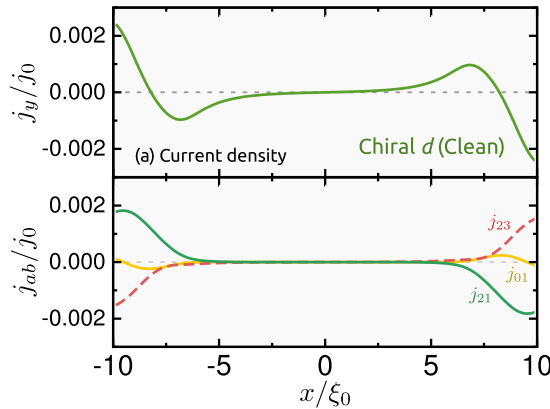


FIG. 6. Results for a chiral d -wave disk with a specular surface obtained by the self-consistent simulation under $\mathbf{A}(\mathbf{r}) = 0$: current density j_y (a) and dominant components j_{ab} (b). The results are plotted in the same manner as Fig. 5.

est Matsubara frequency ω_0 . We have confirmed that the components at higher Matsubara frequencies have the spatial distributions similar to j_{ab} at ω_0 and their amplitudes are smaller than that of j_{ab} . Reflecting the signs of I_{ab} in Fig. 2, j_{01} and j_{23} flow in the clockwise direction, whereas j_{23} and j_{43} do in the counterclockwise one. The magnitudes of j_{01} is slightly larger than j_{21} . As a consequence, the net edge current flows in the clockwise direction. We have confirmed that another possible j_{ab} are negligible. The current j_{01} is carried by the combination of s -wave Cooper pairs and p_y -wave ones. The currents j_{21} are carried by $d_{x^2-y^2}$ -wave \times p_y -wave Cooper pairs.

All of the Cooper pairs in a chiral p -wave superconductor belong to the spin-triplet symmetry classes in the absence of spin-dependent potentials. Therefore, even-parity pairs induced at the surface have the odd-frequency symmetry because of the anti-symmetry relation derived from the Fermi-Dirac statistics of electrons

$$\hat{f}(\mathbf{r}, \theta, i\omega_n) = -\hat{f}^T(\mathbf{r}, \theta + \pi, -i\omega_n), \quad (23)$$

where T represents the transpose of a matrix and means the commutation of the two spins of a Cooper pair. The odd-parity symmetry accounts the negative sign on the right-hand side of Eq. (23) in a spin-triplet superconductor. On the other hand, the induced spin-triplet even-parity components satisfy Eq. (23) by their frequency dependence. They are so-called odd-frequency Cooper pairs.³⁸ As shown in Fig. 5(b) and Eq. (21), the spontaneous edge currents in chiral superconductors are carried by the combination of the even- and odd-frequency Cooper pairs staying at a surface.

In a chiral d -wave superconductor, Δ_2 is responsible for the formation of the surface ABSs. Correspondingly, the pair potential Δ_1 is slightly enhanced near the surface as shown in Fig. 4(b). The spatial profile of the current is shown in Fig. 6(a). As is the case in the non-self-consistent simulation, there are two edge channels

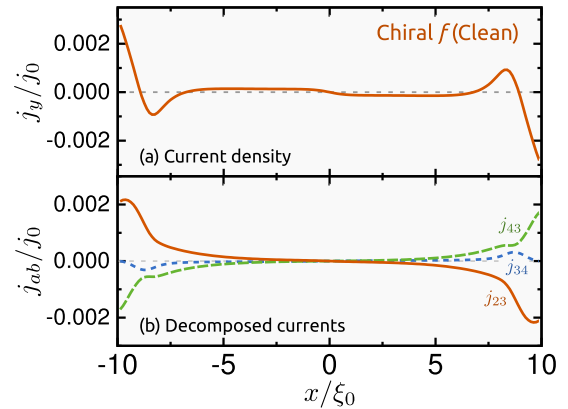


FIG. 7. Results for a chiral f -wave disk with a specular surface obtained by the self-consistent simulation under $\mathbf{A}(\mathbf{r}) = 0$: current density j_y (a) and dominant components j_{ab} (b). The results are plotted in the same manner as Fig. 5.

in a chiral d -wave disk. The current in the clockwise direction flow along the surface and the current in the counterclockwise flow around $x = \pm 7\xi_0$. In Fig. 6(b), we decompose the current into the series of j_{ab} , where we show only dominant components of j_{21} , j_{23} and j_{01} . We note that j_{12} and j_{32} (not shown) have the profile similar to j_{01} , and that another components are negligible. The principal pairing components in a chiral d -wave superconductor are $f_2^c \cos(2\theta)$ and $f_2^s \sin(2\theta)$ as shown in Fig. 2. The spatial variation of the pair potential generates the odd-frequency components $f_1^s \sin(\theta)$ and $f_3^s \sin(3\theta)$. These induced components carry the spontaneous current indicated by j_{21} , j_{23} , j_{12} and j_{32} . As shown in Fig. 6(b), j_{21} and j_{23} flows opposite directions to each other because I_{21} and I_{23} have the opposite signs to each other. As a result, the net edge current becomes smaller than that in a chiral p -wave disk.

In a chiral f -wave disk, Δ_1 is suppressed and Δ_2 is slightly enhanced near the surface due to the emergence of the surface ABSs as shown in Fig. 4(c). The current profile and its decomposition into j_{ab} are shown in Fig. 7(a) and 7(b), respectively. Although the spatial profile of the current is greatly modified by the self-consistent pair potentials, Fig. 7(a) suggests that there are three current channels. Figure 7(b) shows that the spatial dependence of the current components j_{23} , j_{43} and j_{34} are responsible for such complicated current profile. We note that j_{21} and j_{32} (not shown) have almost the same profile as j_{34} .

B. Results under self-consistent pair potential and vector potential

We take into account the vector potential \mathbf{A} induced by the edge current to investigate the Meissner screening effect. The pair potential and the vector potential

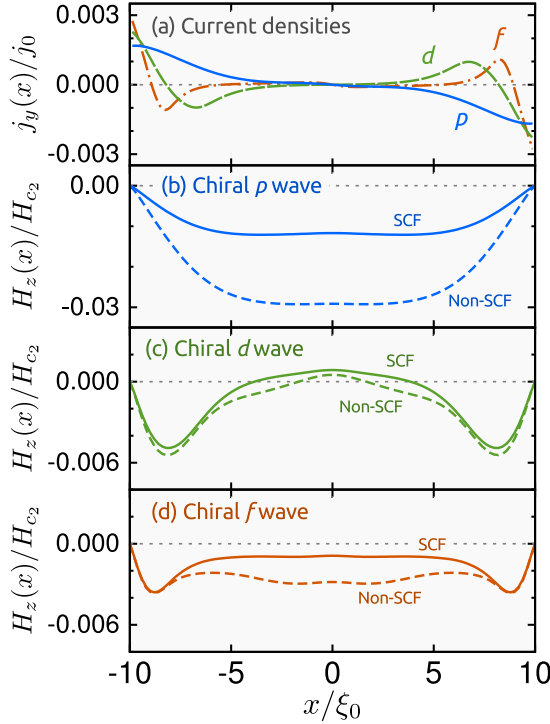


FIG. 8. Current densities in a disk of a chiral superconductor with a specular surface (a). The results are obtained by solving the Eilenberger equation and the Maxwell equation self-consistently and simultaneously. The penetration depth is fixed at $\lambda_L = 5\xi_0$. The other parameters are set to the same values used in Fig. 3. The current densities and the magnetic field are normalized to $j_0 = \hbar c^2/4\pi|e|\xi_0^3 H_{c2} = \hbar c/|e|\xi_0^2$, respectively. In (b)-(d), we compare the spatial distributions of the self-consistent fields (SCF) with those of the non-self-consistent fields (non-SCF). The former is obtained by the current density in (a) by using the relation in Eq. (15). The latter is calculated from the current distributions in Figs. 5(a), 6(a) and 7(a).

are determined in a self-consistent way by solving the Eilenberger equation and the Maxwell equation simultaneously. The spatial profiles of the pair potential are qualitatively the same as those in Fig. 4. The spatial profiles of the chiral edge currents are shown in Fig. 8(a). In Figs. 8(b)-(d), we compare the local magnetic fields obtained under the self-consistent field (SCF) with that under the non-self-consistent field of the vector potential (non-SCF). The latter is calculated from the current distribution in Figs. 5(a), 6(a) and 7(a) with using the relation in Eq. (15).

In a chiral p -wave disk, the Meissner screening by the superconducting condensate suppresses drastically the magnetization as shown in Fig. 8(b). As a result, the amplitude of the current at $x = R$ is less than $0.0017j_0$ under the SCF in Fig. 8(a), whereas it is about $0.008j_0$ under the non-SCF in Fig. 5(a). The magnetic field near the center of a disk remains at finite value because of the finite-size effect in both the SCF and non-SCF sim-

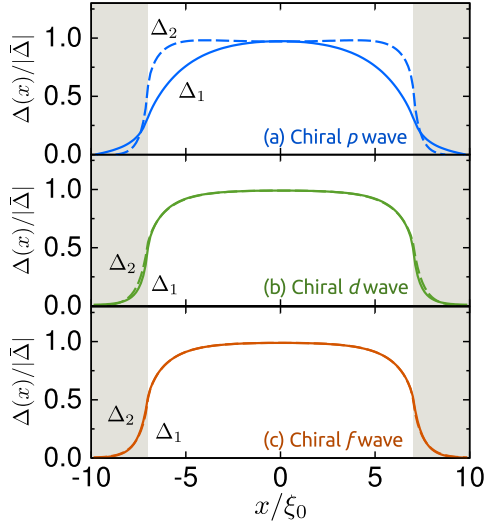


FIG. 9. Pair potentials in a disk of a chiral superconductor with a rough surface as indicated by the shadowed area. The results are obtained by solving the Eilenberger equation self-consistently at $\mathbf{A} = 0$. The parameters are set to the same values used in Fig. 3. The magnetic penetration depth is $\lambda_L = 5\xi_0$.

ulations. At the surface of a semi-infinite chiral p -wave superconductor, we have confirmed that the current distribution under the SCF looks like the results for a chiral d -wave case shown in Fig. 3.¹ Namely, the bulk condensate generates the screening current which flows the opposite direction to that of the chiral current at the surface. As a result, the magnetic field in the bulk region vanishes.

In a chiral d -wave superconductor, the magnetic field is mainly localized around $x = \pm 5\xi_0$ as shown in Fig. 8(c). The results with the SCF is slightly smaller than those with the non-SCF. Thus the Meissner effect in a chiral d -wave disk is much weaker than that in a chiral p -wave one. The current profile under the non-SCF in Fig. 6(a) shows two channels for the edge current. One is the outer channel for the clockwise current and the other is the inner channel for the counterclockwise current. The induced magnetic field by the inner current well screens that by the outer current intrinsically. Such self-screening effect makes the Meissner screening effect weak in a chiral d -wave disk. Actually such characteristic current profile with the non-SCF in Fig. 6(a) are well preserved in the results under the SCF in Fig. 8(a). The current amplitude at the surface $x = R$ reaches to about $0.0024j_0$ in Fig. 8(a) and it is about $0.0027j_0$ in Fig. 6(a). Thus, in a chiral d -wave disk, the Meissner effect modifies the edge current only slightly as shown in Fig. 8(c).

The result of the edge current for a chiral f -wave superconductor in Fig. 8(d) can be explained in the same way. There are three channels for the edge current in a chiral f -wave case as discussed in Fig. 7(a). The self-

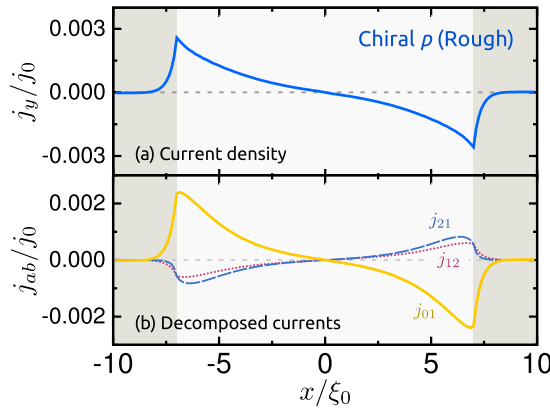


FIG. 10. Results for a chiral p -wave disk with a rough surface obtained by the self-consistent simulation at $\mathbf{A}(\mathbf{r}) = 0$. The current density $j_y(x)$ at $y = 0$ in Eq. (20) is shown in (a). The dominant components j_{ab} at the lowest Matsubara frequency are shown in (b).

screening effect also works well in this case. The characteristic behaviors of the edge current under the non-SCF in Fig. 7(a) totally remain unchanged even under the SCF as shown in Fig. 8(a). The magnetic field around the center of a disk is suppressed by the Meissner effect as shown in Fig. 8(d).

V. DISK WITH A ROUGH SURFACE

In this section, we discuss the effects of a rough surface on the chiral edge currents. The width of the disordered region (shadowed in Fig. 1) is set to be $W = 3\xi_0$ because the chiral edge current in the clean limit mainly flows such area as shown in Fig. 8(a). The strength of roughness is set to $\xi_0/\ell = 1.0$, where $\ell = v_F\tau_0$ is the elastic mean free path of a quasiparticle. The other parameters are set to the same values used in Fig. 5. The rough surface drastically changes the spatial profile of the pair potential and that of induced subdominant pairing components. Thus we first summarize symmetry of Cooper pairs appearing near the rough surface in Sec. V A. Then we discuss briefly the Meissner screening effect by the bulk condensate in Sec. V B.

A. Results under self-consistent pair potential at $\mathbf{A} = 0$

Here we discuss the results obtained by solving *only* the Eilenberger equation under the condition $\mathbf{A} = 0$ in Eq. (3). We obtain the self-consistent solutions of $\Delta_1(\mathbf{r})$, $\Delta_2(\mathbf{r})$, and $\hat{\Sigma}(\mathbf{r}, i\omega_n)$. The pair potentials are presented in Fig. 9. The surface roughness strongly suppressed the pair potentials Δ_1 and Δ_2 in the disordered region of a chiral p -wave disk. At the interface between the dis-

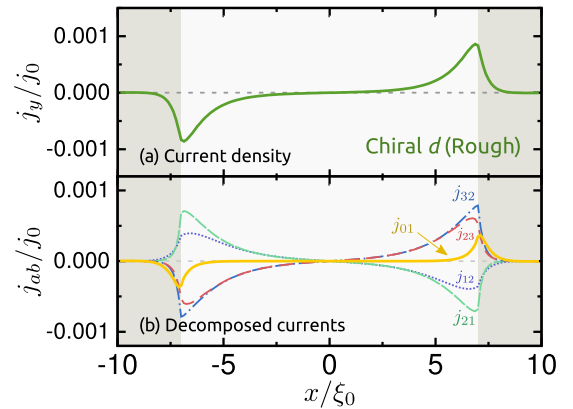


FIG. 11. Results for a chiral d -wave disk with a rough surface obtained by the self-consistent simulation at $\mathbf{A}(\mathbf{r}) = 0$: current density j_y (a) and dominant components j_{ab} (b). The results are plotted in the same manner as Fig. 10.

ordered and clean regions (we refer to it as the d/c interface in what follows), Δ_1 is suppressed more significantly than Δ_2 , which suggests the formation of the ABSs there.²² We show the current density j_y at $y = 0$ and the dominant current components j_{ab} in Fig. 10. Comparing Fig. 5(a) with 10(a), one can find that the peak of the edge current moves from the surface to the d/c interface, and that its maximum value $0.0028j_0$ is comparable to the maximum value in the clean limit. As shown in Fig. 10(b), the edge current in a chiral p -wave disk is mainly carried by three components; j_{01} , j_{21} , and j_{12} . Among them, the combination of s -wave $\times p_y$ -wave pairs (j_{01}) dominates obviously the chiral current in a disk with a rough surface. The spatial variation in Δ_1 generates the s -wave and $d_{x^2-y^2}$ -wave odd-frequency pairs.²⁴ The induced s -wave pairs, in particular, are robust even under the random potential. Such property supports the robustness of the chiral edge current in a chiral p -wave superconductor.

The edge current in a chiral d -wave disk shows a qualitatively different behavior from that in a chiral p -wave case. As shown in Fig. 11(a), the chiral current in a disordered disk flows only in the counterclockwise direction. This behavior can be understood by comparing the current profiles in Fig. 6(a) with those in Fig. 11(a). In the clean disk, there are two edge currents: the outer current running in the clockwise direction and the inner current running in the counterclockwise one as shown in Fig. 6(a). The surface roughness eliminates the outer current channel. The inner current channel, however, remains even in the presence of the surface roughness and are responsible for the chiral current in the counterclockwise direction. We have confirmed that the inner current can survive under much stronger roughness such as $\xi_0/\ell \sim 30$. The decomposed components of the current j_{ab} are shown in Fig. 11(b). The edge current is mainly carried by the five combinations: j_{01} , j_{12} , j_{21} , j_{23} , and j_{32} . The four com-

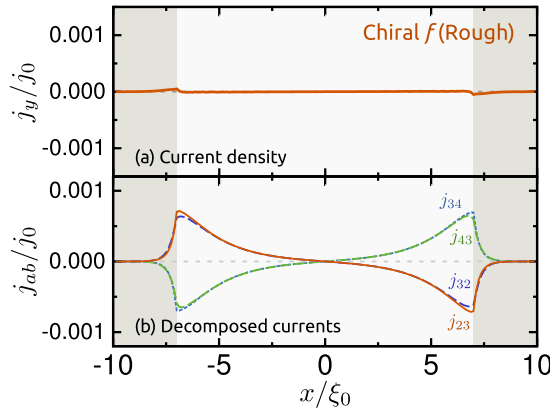


FIG. 12. Results for a chiral f -wave disk with a rough surface obtained by the self-consistent simulation at $\mathbf{A}(\mathbf{r}) = 0$: current density j_y (a) and dominant components j_{ab} (b). The results are plotted in the same manner as Fig. 10.

ponents j_{12} , j_{21} , j_{23} , and j_{32} almost cancel one another. As shown in Fig. 9(b), the surface roughness suppresses both Δ_1 and Δ_2 in the same manner near the shadowed area, which results in

$$f_2^c(x) \simeq f_2^s(x). \quad (24)$$

The spatial variation of Δ_1 generates mainly $f_1^c \cos(\theta)$ and $f_3^c \cos(2\theta)$ with $f_1^c(x) \simeq f_3^c(x)$. In the same way, the spatial variation of Δ_2 induces $f_1^s \sin(\theta)$ and $f_3^s \sin(3\theta)$ with $f_1^s(x) \simeq f_3^s(x)$. Therefore, the relation

$$f_1^c(x) \simeq f_3^c(x) \simeq f_1^s(x) \simeq f_3^s(x), \quad (25)$$

holds among the four coefficients. By applying the relation in Eqs. (24) and (25) into Eq. (21) with the I_{ab} in Fig. 2, we can conclude that j_{21} cancels j_{32} and j_{12} cancels j_{23} . The remaining component j_{01} , the contribution from the s -wave $\times p_y$ -wave pairs, dominates the edge current. Because s -wave Cooper pairs are robust against the roughness, j_{01} can exist even under much stronger disordered potential. We have confirmed that j_{01} appears only in a small disk-shaped superconductor and is absent near the d/c interface in a semi-infinite superconductor.

As shown in Fig. 12(a), the edge current in a chiral f -wave disk with a rough surface becomes almost zero in this scale of the plot (i.e., $|j_y| \ll j_0$). Within the accuracy of our numerical simulation, the maximum value of the current density is less than $5 \times 10^{-5} j_0$. The dominant components j_{23} , j_{32} , j_{34} , and j_{43} are shown in Fig. 12(b). As shown in Fig. 9(c), the surface roughness suppresses both Δ_1 and Δ_2 in the same manner near the shadowed area. By applying the same logic used in a chiral d -wave case, it is possible to show the relations

$$f_3^c(x) \simeq f_3^s(x), \quad (26)$$

$$f_2^c(x) \simeq f_4^c(x) \simeq f_2^s(x) \simeq f_4^s(x). \quad (27)$$

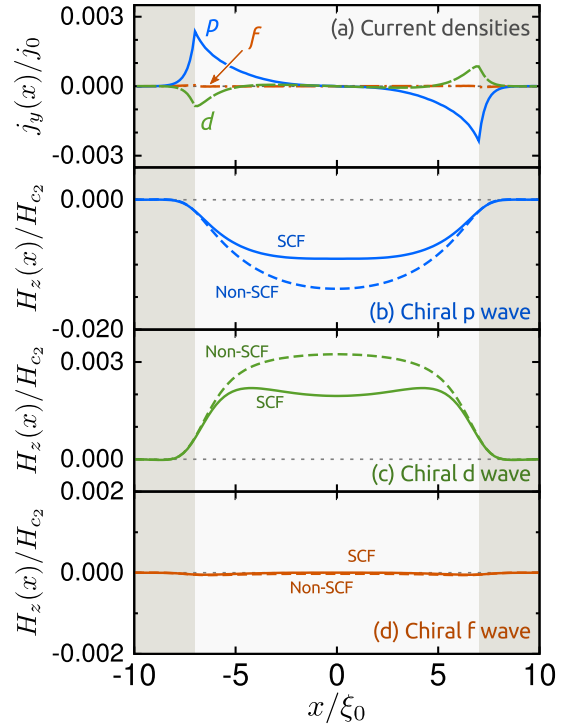


FIG. 13. (a) Current densities in a disk of a chiral superconductor with a rough surface. The results are obtained by solving the Eilenberger equation and the Maxwell equation self-consistently and simultaneously. (b)-(d) Comparison of the SCF with the non-SCF. The strength of the disorder and the width of the disordered region is set to $\xi_0/\ell = 1$ and $W = 3\xi_0$, respectively. The other parameters are set to the same values used in Fig. 8.

These relations and I_{ab} in Fig. 2 explain the cancellation among the current components such as $j_{23} + j_{34} \simeq 0$ and $j_{32} + j_{43} \simeq 0$. As a result, the net edge current totally disappears as shown in Fig. 12(a).

B. Results under self-consistent pair potential and vector potential

We discuss the effects of self-induced vector potential on the chiral current in a disk with a rough surface. By solving simultaneously the Eilenberger and the Maxwell equations, we obtain the self-consistent solutions of $\Delta_1(\mathbf{r})$, $\Delta_2(\mathbf{r})$, $\mathbf{A}(\mathbf{r})$, and $\hat{\Sigma}(\mathbf{r}, i\omega_n)$. Here we do not show the pair potentials because they remain unchanged from those in Fig. 9 even quantitatively. The results of the edge currents are shown in Fig. 13(a). The spatial distributions of the magnetic field are presented in Figs. 13(b)-(d). For comparison, we show the magnetic field under the non-SCF calculated from the current profiles of Figs. 10(a), 11(a) and 12(a) by applying the relation in Eq. (15).

As shown in Fig. 13(b), the Meissner effect suppresses

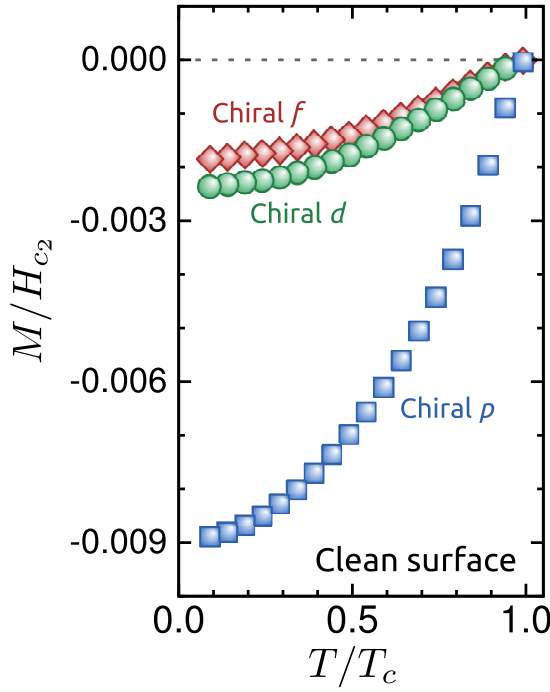


FIG. 14. Temperature dependences of the spontaneous magnetization of a small chiral superconductor with a specular surface. The magnetization is defined by Eq. (16) and is normalized to the second critical magnetic field H_{c2} .

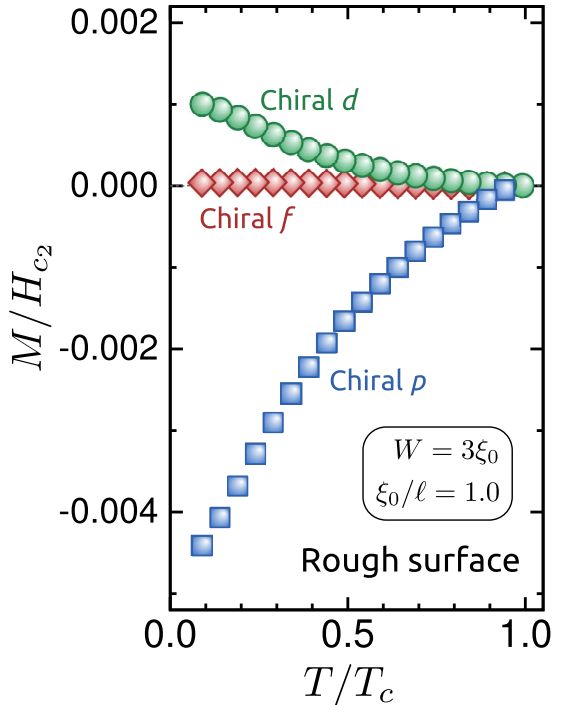


FIG. 15. Temperature dependences of the spontaneous magnetization of a small chiral superconductor with a rough surface. The parameters related to the roughness are set to $\xi_0/\ell = 1.0$ and $W = 3\xi_0$.

the magnetic field around the center of a chiral p -wave disk. When we compare the results for a chiral p -wave disk under the SCF in Fig. 13(a) and those with the non-SCF in Fig. 10(a), the current profile in Fig. 13(a) is spatially compressed into narrower region by the Meissner effect.

The similar features are found also in the results of a chiral d -wave disk as shown in Fig. 13(c). In the presence of the surface roughness, the current profile under the non-SCF has a monotonic spatial dependence between the center of the disk and the d/c interface as presented in Fig. 11(a). Therefore, the self-screening effect observed in a clean disk does not work at all. In a chiral d -wave disk with a rough surface, the Meissner effect becomes stronger than that in a disk with a specular surface. The Meissner effect suppresses the magnetization near the center of the disk as shown in Fig. 13(c).

In a chiral f -wave disk, the surface roughness strongly suppresses the chiral current. Thus the magnetic field is much smaller than H_{c2} everywhere in the disk as shown in Fig. 13(d). Within the numerical accuracy, the magnetic field is less than $7 \times 10^{-5} H_{c2}$ in our simulation.

VI. TEMPERATURE DEPENDENCES OF SPONTANEOUS MAGNETIZATION

Finally, we discuss the dependences of the spontaneous magnetization on temperature which are measurable values in experiments. The simulation is started at $T \simeq T_c$ with a homogeneous pair potential $\Delta_1(\mathbf{r}) = \Delta_2(\mathbf{r}) = |\bar{\Delta}(T)|$ and without any external magnetic fields. The magnitude of a spontaneous magnetization is defined in Eq. (16). In the simulations, the pair potential, the impurity self-energy, and the vector potential are calculated self-consistently. The results in a disk with a specular surface are shown in Fig. 14. At a low temperature $T = 0.1T_c$, the magnetization of a chiral p -wave disk reaches to about $0.009H_{c2}$. In chiral d - and f -wave disks, the magnetizations are about $0.002H_{c2}$. Although the magnetization decreases with increasing the radius of a disk by its definition Eq. (16), $0.002H_{c2}$ at $R = 10\xi_0$ would be detectable value in experiments. The results in a disk with a rough surface are shown in Fig. 15, we choose $\xi_0/\ell = 1.0$ and $W = 3\xi_0$. In a chiral p -wave superconductor, the amplitude of the magnetization is smaller than the results in the clean limit at all of the temperatures. As we discussed in Sec. V, however, the amplitude of the current density in a disk with a rough surface is comparable to that in a disk with a specular surface. In Eq. (16), the magnetization is normalized by

the area of a whole superconducting disk. As shown in Fig. 9, however, the effective radius of the superconducting region shrinks down to $R - W$ in the presence of the roughness. When we renormalize the magnetization by the effective superconducting area, the renormalized magnetization $\tilde{M} = MR^2/(R-W)^2 \approx 2M$ is comparable to the magnetization in the clean disk. This fact means the robustness of the chiral current in the presence of the surface roughness.

In a chiral d -wave disk, the sign of the magnetization in Fig. 15 changes from that in Fig. 14 because only the inner chiral edge channel survives in a disk with a rough surface and flows the current in the counterclockwise direction. We have confirmed that the magnetization of a chiral d -wave disk becomes small but remains finite even under the much stronger disorder (e.g., $\xi_0/\ell = 30$). As discussed in Sec. V A, the combination of s -wave and p_y -wave Cooper pairs carry the spontaneous current in both a chiral p -wave disk and a chiral d -wave one. Therefore, the degree of the robustness against the surface roughness is a common feature in the two superconductors. In the case of a chiral f -wave superconductor, the amplitude of the magnetization is almost zero in the scale of Fig. 15. Within the numerical accuracy, we estimate that the magnetization is smaller than $4 \times 10^{-5} H_{c2}$. In experiments, the chiral edge current in Sr_2RuO_4 has never been observed yet. Our results implies a possibility of chiral f -wave symmetry in Sr_2RuO_4 .

VII. CONCLUSION

We have studied the effects of the surface roughness on the spontaneous edge current in small chiral superconductors characterized by chiral p -, chiral d - and chiral f -wave pairing symmetries. On the basis of the quasiclassical Eilenberger formalism, we numerically calculate the chiral current and the spontaneous magnetization of the small superconducting disk. By solving the Eilenberger equation and the Maxwell equation simultaneously, we obtain the self-consistent solutions of the pair potential, the impurity self-energy, and the vector potential. To understand the physics behind the complicated current distribution in real space, we decompose the current into a series of components in terms of the symmetry of a Cooper pair. The chiral edge current carried by a combination of two pairing components: the even-parity component and the odd-parity component. In a spin-singlet (spin-triplet) superconductor, the odd-parity (the even-parity) Cooper pairs have the odd-frequency symmetry.

The effects of the surface roughness depends on the pairing symmetry of a superconductor. The chiral current is robust under the surface roughness in a chiral p - and chiral d -wave symmetries. In a chiral p -wave symmetry, the characteristic features of the chiral current are insensitive to the surface roughness. In a chiral d -wave symmetry, the chiral current changes its direction due to the surface roughness. In both the chiral p -wave

and chiral d -wave cases, the chiral current is carried by the combination of two pairing correlations. One is the correlation with p -wave symmetry and the other is the correlation with s -wave symmetry. The Meissner screening effect by the bulk condensate reduces the spontaneous magnetization. The resulting amplitude of the magnetization, however, is still large enough to be detected in experiments. In a chiral f -wave superconductor, the surface roughness suppresses significantly the spontaneous edge current.

So far the absence of the spontaneous magnetization in strontium ruthenate is attributed mainly to the rough surface of a sample. However, we conclude that the edge current in a chiral p -wave superconductor is robust under the roughness at the surface. If the single-band model well describes the essential properties of the superconducting phase, the spontaneous magnetization could be observed in experiments. Or a strontium ruthenate might have a possibility of chiral f -wave symmetry.

ACKNOWLEDGMENTS

The authors are grateful to Y. Maeno, A. A. Golubov, Y. Tanaka, S. Kashiwaya, Ya. V. Fominov, and M. Yu. Kupriyanov for useful discussions. This work was supported by Topological Materials Science (No. 15H05852) and KAKENHI (Nos. 26287069 and 15H03525) from the Ministry of Education, Culture, Sports, Science and Technology (MEXT) of Japan, and by the Ministry of Education and Science of the Russian Federation (Grant No. 14Y.26.31.0007). S.-I. S. is supported in part by Grant-in-Aid for JSPS Fellows (Grant No. 15J00797) by Japan Society for the Promotion of Science (JSPS).

Appendix A: Analysis of chiral edge currents by the Bogoliubov-de Gennes formalism

The chiral edge current can be analyzed by the Bogoliubov-de Gennes (BdG) formalism. The BdG equation in momentum space is given by

$$\begin{bmatrix} \hat{\xi}_k & \hat{\Delta}_k \\ \hat{\Delta}_k^\dagger & -\hat{\xi}_k \end{bmatrix} \begin{bmatrix} \hat{u}_k \\ \hat{v}_k \end{bmatrix} = E_k \begin{bmatrix} \hat{u}_k \\ \hat{v}_k \end{bmatrix}, \quad (\text{A1})$$

where $\hat{\xi}_k = (\hbar^2 k^2/2m - \mu)\hat{\sigma}_0$ with $k = |\mathbf{k}|$. The spin structure of the pair potential $\hat{\Delta}_k$ and that of the wave functions \hat{u}_k and \hat{v}_k are represented by

$$\hat{\Delta}_k = \begin{cases} \Delta_k \hat{\sigma}_1 & \text{for a spin triplet} \\ \Delta_k i\hat{\sigma}_2 & \text{for a spin singlet,} \end{cases} \quad (\text{A2})$$

$$\hat{u}_k = u_k \hat{\sigma}_0, \quad (\text{A3})$$

$$\hat{v}_k = \begin{cases} v_k \hat{\sigma}_1 & \text{for a spin triplet} \\ v_k (i\hat{\sigma}_2)^\dagger & \text{for a spin singlet.} \end{cases} \quad (\text{A4})$$

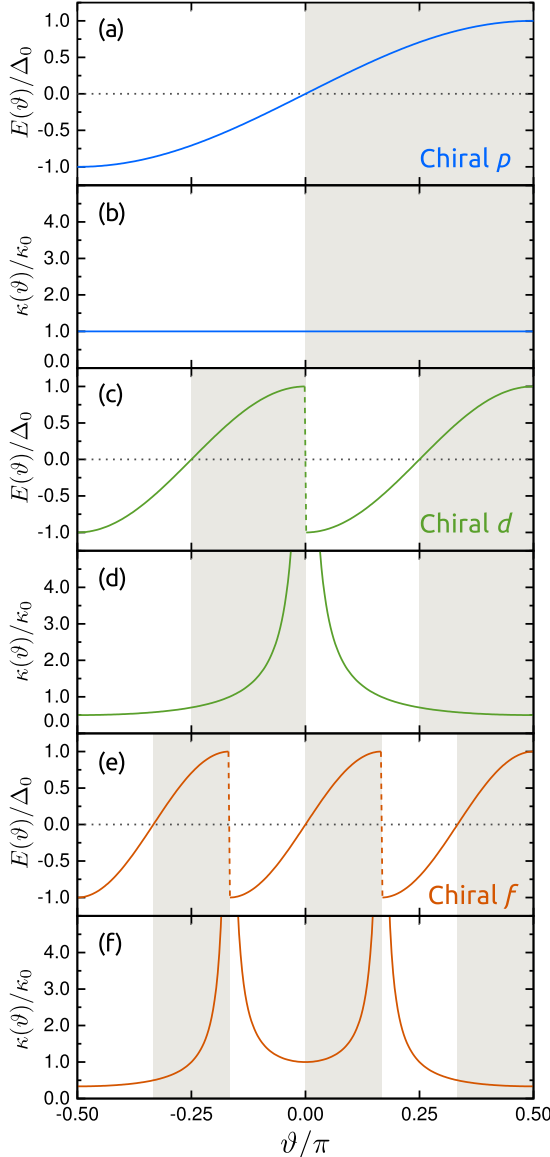


FIG. 16. Dispersion relations of the edge states and angle-dependent decay lengths. The results for chiral p -wave, d -wave, and f -wave superconductors are shown in (a) and (b), (c) and (d), and (e) and (f), respectively. The shadowed areas indicate the interval of summation in Eq. (A12) with $k_y = k_F \sin \vartheta$.

As a result, we can reduce the BdG equation from a 4×4 matrix structure to a 2×2 one as

$$\begin{bmatrix} \xi_{\mathbf{k}} & \Delta_{\mathbf{k}} \\ \Delta_{\mathbf{k}}^* & -\xi_{\mathbf{k}} \end{bmatrix} \begin{bmatrix} u_{\mathbf{k}} \\ v_{\mathbf{k}} \end{bmatrix} = E_{\mathbf{k}} \begin{bmatrix} u_{\mathbf{k}} \\ v_{\mathbf{k}} \end{bmatrix}. \quad (\text{A5})$$

In the BdG formalism, the pair potential for chiral superconductors is represented as $\Delta_{\mathbf{k}} = \Delta_0 e^{i\chi\vartheta}$, where Δ_0 is the amplitude of the pair potential, ϑ is defined as $k_x = k_F \cos \vartheta$ and $k_y = k_F \sin \vartheta$ with k_F being the Fermi wave number. The chiral p -wave, d -wave, and f -wave pairings correspond to $\chi = 1, 2$, and 3 , respectively. The

chiral edge current is given by

$$J_y = \frac{\hbar e}{2im} \sum_{\sigma} [\psi_{\sigma}^{\dagger} \partial_y \psi_{\sigma} - \partial_y \psi_{\sigma}^{\dagger} \psi_{\sigma}], \quad (\text{A6})$$

where $\psi_{\sigma} = \psi_{\sigma}(\mathbf{r})$ and $\psi_{\sigma}^{\dagger} = \psi_{\sigma}^{\dagger}(\mathbf{r})$ is the annihilation and the creation operator of an electron with spin σ , $e < 0$ is the charge of an electron.

We consider a semi-infinite superconductor which occupies $x > 0$ and the periodic boundary condition in the y direction.² Under this condition, all of the states characterized by k_y . To find the edge bound states, we focus on the wave function with $|E(k_y)| < \Delta_0$. The edge states $\Psi^E(\mathbf{r}) = [u_{k_y}(x) \ v_{k_y}(x)]^T$ must satisfy the boundary conditions: $\Psi^E(\mathbf{r})|_{x=0} = 0$ and $\Psi^E(\mathbf{r})|_{x \rightarrow \infty} \rightarrow 0$. As a consequence, we can find the energy dispersion of the edge states for each superconductor as

$$E(\vartheta) = \begin{cases} \Delta_0 \zeta_{\chi} \sin(\chi\vartheta) & \text{for a triplet,} \\ -\Delta_0 \zeta_{\chi} \cos(\chi\vartheta) & \text{for a singlet,} \end{cases} \quad (\text{A7})$$

with

$$\zeta_{\chi} = \begin{cases} \text{sgn}[\cos(\chi\theta)] & \text{for a triplet,} \\ \text{sgn}[\sin(\chi\theta)] & \text{for a singlet,} \end{cases} \quad (\text{A8})$$

and the wave function of the edge state takes the form

$$\begin{bmatrix} u_{k_y}(x) \\ v_{k_y}(x) \end{bmatrix} = \sqrt{\frac{2}{\kappa(\vartheta)}} e^{-x/\kappa(\vartheta)} i \sin(k_x x) \Phi_{\chi}, \quad (\text{A9})$$

with

$$\Phi_{\chi} = \begin{cases} [\zeta_{\chi} e^{i\pi/4} \ e^{-i\pi/4}]^T & \text{for a triplet,} \\ [\zeta_{\chi} \ 1]^T & \text{for a singlet,} \end{cases} \quad (\text{A10})$$

where we use the approximation $\Delta_0 \ll \mu$. The decay length $\kappa(\vartheta)$ depends on the pairing symmetry

$$\kappa(\vartheta) = \begin{cases} \kappa_0 & \text{for } \chi = 1, \\ \kappa_0/|2 \sin \vartheta| & \text{for } \chi = 2, \\ \kappa_0/|1 - 4 \sin^2 \vartheta| & \text{for } \chi = 3, \end{cases} \quad (\text{A11})$$

where $\kappa_0 = \hbar v_F / \Delta$. The dispersion relations and the angle-dependent decay length are shown in Fig. 16. In a chiral p -wave superconductor, there is one branch and $\kappa(\vartheta)$ dose not depend on ϑ . In chiral d - and f -wave superconductors, there are two and three branches and $\kappa(\vartheta)$ depends on the angle ϑ .

Using the wave function of the edge states, we can extract the electron field operators of the edge states $\Psi^E = [\bar{\psi}_{\uparrow}(\mathbf{r}) \ \bar{\psi}_{\downarrow}^{\dagger}(\mathbf{r})]^T$ as

$$\Psi^E = \sum'_{k_y} \begin{bmatrix} u_{k_y}(x) & s_{\nu} v_{-k_y}^*(x) \\ v_{k_y}(x) & u_{-k_y}^*(x) \end{bmatrix} \begin{bmatrix} \gamma_{k_y} \\ \gamma_{-k_y}^{\dagger} \end{bmatrix} \frac{e^{ik_y y}}{\sqrt{w}}, \quad (\text{A12})$$

where γ_{k_y} ($\gamma_{k_y}^{\dagger}$) is the annihilation (creation) operator of the Bogoliubov quasiparticle, and w is the width of

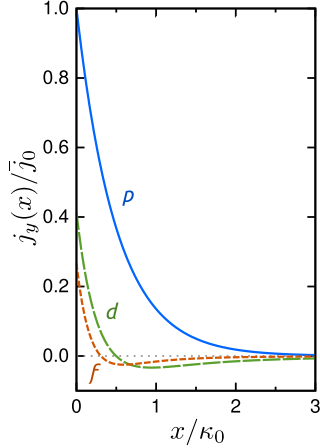


FIG. 17. Spatial dependences of the chiral edge currents. The results are obtained by the Bogoliubov-de Gennes formalism. We use the approximation $\kappa_0 k_F \gg 1$. The currents are normalized to $\bar{j}_0 = 4|e|\mu/\pi\hbar$. These results are consistent with those in Fig. 3. In the chiral p -wave superconductor, the edge current monotonically decreases. In the chiral d -wave and the chiral f -wave, there are regions with $j_y < 0$ even though we do not consider the Meissner effect.

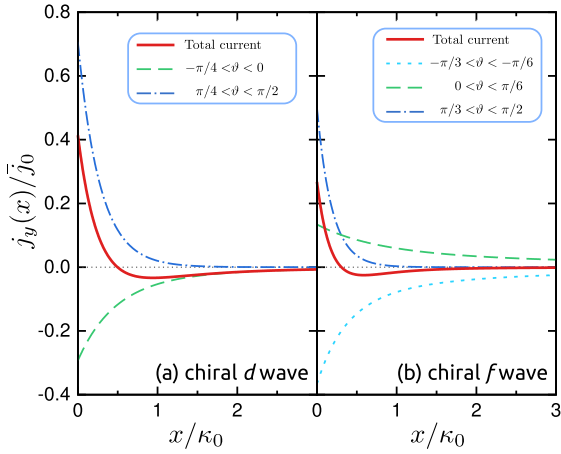


FIG. 18. Contributions from each of the branches to the total edge current in (a) chiral d -wave and (b) chiral f -wave superconductors. At the zero temperature, the interval of the integration is determined uniquely. We decompose the total current into each contribution from the branches.

a superconductor in the y direction. The summation in Eq. (A12) is restricted to k_y with $E(k_y) \geq 0$ in or-

der to avoid overcounting, where $k_y = k_F \sin \vartheta$. The corresponding intervals of summation are shadowed in Fig. 16. In the ground states, the Bogoliubov operator obeys $\gamma_{k_y} |0\rangle$.

At the zero temperature, the chiral edge current becomes

$$j_y(x) = \frac{1}{w} \int dy \langle 0 | J_y | 0 \rangle \quad (A13)$$

$$= \frac{2\hbar|e|}{mw} \sum_{k_y} k_y |v_{k_y}(x)| \quad (A14)$$

$$= \frac{2\hbar|e|}{mw} \sum_{k_y} \frac{2k_y}{\kappa(k_y)} e^{-2x/\kappa(k_y)} \sin^2(k_x x) \quad (A15)$$

$$= \frac{4|e|\mu}{\pi\hbar} \int' d(\sin \vartheta) \frac{\sin \vartheta}{\kappa(\vartheta)} e^{-2x/\kappa(\vartheta)} \sin^2(k_x x) \quad (A16)$$

where we use $\mu = \hbar^2 k_F^2 / 2m$. The spatial dependences of the chiral edge current are shown in Fig. 17, where we use the relation $\kappa_0 k_F \gg 1$ and the current densities are normalized to $\bar{j}_0 = 4|e|\mu/\pi\hbar$. In a chiral p -wave superconductor, the edge current decreases monotonically from the edge. In chiral d -wave and f -wave superconductors, there is a region where $j_y(x) < 0$.

To study the characteristic spatial distribution of the chiral current, we decompose the current into the contributions from each branch. The result for a chiral d -wave superconductor is shown in Fig. 18(a). The intervals of the integration in Eq. (A16) are $-\pi/4 \leq \vartheta \leq 0$ and $\pi/4 \leq \vartheta \leq \pi/2$. In the former interval, the edge state carries a current in the $-y$ direction. In the latter interval, on the other hand, the edge state carries a current in the $+y$ direction as shown in Fig. 18(a). In addition, the decay length for $-\pi/4 \leq \vartheta \leq 0$ is longer than that for $\pi/4 \leq \vartheta \leq \pi/2$ as shown in Fig. 17(d). As a result, the total current density shows such a characteristic spatial dependence. In a chiral f -wave superconductor, there are three branches. Two branches carry currents in the $+y$ direction. The remaining one branch carries a current in the $-y$ direction. As a consequence, the edge current of a chiral f -wave superconductor shows the complicated spatial distribution.

The results in this Appendix are qualitatively the same as the results calculated in the non-self-consistent simulations of the Eilenberger equation shown in Fig. 3. Here the chiral current is calculated from a quasiparticle point of view. In the text, the characteristic feature of the chiral current is discussed from a view point of a Cooper pair.

¹ M. Matsumoto, M. Sigrist. J. Phys. Soc. Jpn. **68**, 994 (1999).

² A. Furusaki, M. Matsumoto, and M. Sigrist. Phys. Rev. B **64**, 054514 (2001).

³ Y. Maeno, H. Hashimoto, K. Yoshida, S. Nishizaki, T. Fu-

jita, J.G. Bednorz, F. Lichtenberg, Nature **372**, 532 (1994).

⁴ A. P. Mackenzie, Y. Maeno, Reviews of Modern Physics **75**, 657 (2003).

⁵ K. Takeda, H. Sakurai, E. Takayama-Muromachi, F. Izumi, R. A. Dilanian, T. Sakai, Nature **422** 53 (2003).

⁶ G. Baskaran, Phys. Rev. Lett. **91**, 097003 (2003).

⁷ M. Ogata, J. Phys. Soc. Jpn. **72**, 1839 (2003).

⁸ A. Tanaka and X. Hu, Phys. Rev. Lett. **91**, 257006 (2003).

⁹ R. Nandkishore, L. S. Levitov, A.V. Chubukov, Nature Physics **8**, 158 (2012).

¹⁰ M. L. Kiesel, C. Platt, W. Hanke, D. A. Abanin, and R. Thomale, Phys. Rev. B **86**, 020507(R) (2012).

¹¹ M. L. Kiesel, C. Platt, W. Hanke, and R. Thomale, Phys. Rev. Lett. **111**, 097001 (2013).

¹² M. H. Fischer, T. Neupert, C. Platt, A. P. Schnyder, W. Hanke, J. Goryo, R. Thomale, and M. Sigrist, Phys. Rev. B **89**, 020509(R)

¹³ Y. Kasahara, H. Shishido, T. Shibauchi, Y. Haga, T. D. Matsuda, Y. Onuki, and Y. Matsuda, New Journal of Physics, **11**, 055061 (2009).

¹⁴ H. Kusunose, J. Phys. Soc. Jpn. **81**, 023704 (2012).

¹⁵ Y. Tada, W. Nie, and M. Oshikawa, Phys. Rev. Lett. **114**, 195301 (2015).

¹⁶ W. Huang, E. Taylor, and C. Kallin, Phys. Rev. B **90**, 224519 (2014).

¹⁷ P. G. Björnsson, Y. Maeno, M. E. Huber, and K. A. Moler, Phys. Rev. B **72**, 012504 (2005).

¹⁸ J. R. Kirtley, C. Kallin, C. W. Hicks, E.-A. Kim, Y. Liu, K. A. Moler, Y. Maeno, and K. D. Nelson, Phys. Rev. B **76**, 014526 (2007).

¹⁹ K. Saitoh, S. Kashiwaya, H. Kashiwaya, M. Koyanagi, Y. Mawatari, Y. Tanaka, and Y. Maeno, Appl. Phys. Express **5**, 113101 (2012).

²⁰ K. Saitoh, S. Kashiwaya, H. Kashiwaya, Y. Mawatari, Y. Asano, Y. Tanaka, and Y. Maeno, Phys. Rev. B **92**, 100504(R) (2015).

²¹ P. E. C. Ashby and C. Kallin, Phys. Rev. B **79**, 224509 (2009).

²² S. V. Bakurskiy, A. A. Golubov, M. Yu. Kupriyanov, K. Yada, and Y. Tanaka, Phys. Rev. B **90**, 064513 (2014).

²³ S.-I. Suzuki and Y. Asano, Phys. Rev. B **89**, 184508 (2014).

²⁴ S.-I. Suzuki and Y. Asano, Phys. Rev. B **92**, 214510 (2015).

²⁵ L. J. Buchholtz and G. Zwicknagl, Phys. Rev. B **23**, 5788 (1981).

²⁶ J. Hara and K. Nagai, Progress of Theoretical Physics **74**, 1237 (1986).

²⁷ S. Kashiwaya, Y. Tanaka, N. Terada, M. Koyanagi, S. Ueno, L. Alff, H. Takashima, Y. Tanuma, K. Kajimura, Journal of Physics and Chemistry of Solids **59** 2034 (1998).

²⁸ C.R. Hu, Phys. Rev. Lett. **72**, 1526 (1994).

²⁹ Y. Tanaka and S. Kashiwaya, Phys. Rev. Lett. **74**, 3451 (1995).

³⁰ Y. Asano, Y. Tanaka, and S. Kashiwaya, Phys. Rev. B **69** 134501 (2004).

³¹ G. Eilenberger, Z. Phys. **214**, 195 (1968).

³² J. A. Sauls, Phys. Rev. B **84**, 214509 (2011).

³³ K. Nagai, J. Low Temp. Phys. **175**, 44 (2014).

³⁴ N. Schopohl and K. Maki, Phys. Rev. B **52**, 490 (1995).

³⁵ N. Schopohl, arXiv:cond-mat/9804064.

³⁶ M. Eschrig, Phys. Rev. B **80**, 134511 (2009).

³⁷ Y. Nagai, K. Tanaka, and N. Hayashi, Phys. Rev. B **86**, 094526 (2012).

³⁸ V. L. Berezinskii, Pis'mav Zh. Eksp. Teor. Fiz. **20**, 628 (1974), [JETP Lett. **20**, 287 (1974)].